A reappraisal of the ink-bottle effect and pore structure of cementitious materials using intrusion-extrusion cyclic mercury porosimetry

Zhang, Yong; Wu, Kai; Yang, Zhengxian; Ye, Guang

DOI
10.1016/j.cemconres.2022.106942

Publication date
2022

Document Version
Final published version

Published in
Cement and Concrete Research

Citation (APA)
Zhang, Y., Wu, K., Yang, Z., & Ye, G. (2022). A reappraisal of the ink-bottle effect and pore structure of cementitious materials using intrusion-extrusion cyclic mercury porosimetry. *Cement and Concrete Research*, *161*, Article 106942. https://doi.org/10.1016/j.cemconres.2022.106942

Cement and Concrete Research 161 (2022) 106942

Contents lists available at ScienceDirect

Cement and Concrete Research

journal homepage: www.elsevier.com/locate/cemconres

A reappraisal of the ink-bottle effect and pore structure of cementitious materials using intrusion-extrusion cyclic mercury porosimetry

Yong Zhang [a,b], Kai Wu [c], Zhengxian Yang [a,*], Guang Ye [b,*]

[a] College of Civil Engineering, Fuzhou University, Fuzhou 350116, China
[b] Microlab, Section of Materials and Environment, Faculty of Civil Engineering and Geosciences, Delft University of Technology, 2628 CN Delft, the Netherlands
[c] Key Laboratory of Advanced Civil Engineering Materials of Ministry of Education, School of Materials Science and Engineering, Tongji University, Shanghai 201804, China

ARTICLE INFO

Keywords:
Mercury porosimetry
Ink-bottle effect
Connectivity
Pore size distribution
Critical pore diameter

ABSTRACT

Reliable characterization of the pore structure is essentially important for transport-related durability studies of cementitious materials. Mercury intrusion porosimetry has been commonly used for pore structure measurement while the ink-bottle effect significantly affects the trustworthiness of pore size features of cementitious materials. Pressurization-depressurization cycling mercury intrusion porosimetry (PDC-MIP) is an alternative approach previously reported with the purpose to provide better estimates of pore size results. It is found however that the PDC-MIP greatly overestimates the ink-bottle pore volume owing to the incomplete extrusion of mercury in throat pores after the pressurization-depressurization cycle. Intrusion-extrusion cyclic mercury porosimetry (IEC-MIP), as a further improvement, is then described, which can reliably capture the ink-bottle effect and obtain a clear picture of the distribution of the ink-bottle pores in cementitious materials. The ink-bottle effect of cement pastes is observed being pore size-dependent and the role of critical pores is emphasized. Water-cement ratio primarily changes the effective porosity while plays a minor role in the ink-bottle porosity. The addition of reactive blends substantially enhances the ink-bottle effect during mercury penetration into small pores. IEC-MIP tests, together with a unique data analysis, enable to obtain a more truthful pore size distribution.

1. Introduction

Nowadays it is rare for concrete structures to fail due to lack of intrinsic strength. Intensive emphasis has been placed on their expected lives due to gradual degradation caused by lack of durability [1–5]. Penetration of corrosive ions or gases from environment into the pore structure is often recognized as a major reason leading to concrete degradation. Unfortunately, some fundamental aspects of the pore structure characteristics involved in mass transport properties of concrete are imperfectly understood so far and fully interpreting the bulk of experimental data from field concrete samples is far from easy.

Cement powders, together with mineral admixtures in many situations, react with water and a sizeable number of pores spanning several orders of magnitude are formed with various origins. Many technologies and methods have been developed for cementitious pore structure measurements, such as nitrogen sorption [6], mercury intrusion porosimetry [7], scanning electron microscope [8], wood's metal intrusion porosimetry [9], X-ray computed tomography [10], ^{1}H nuclear magnetic resonance relaxometry [11], optical microscopic observation [12], etc. 3D reconstruction with a spatial resolution as high as 30 nm has been reported [13]. Various techniques have different limitations and they are applied often for dissimilar situations. Nitrogen sorption loses its accuracy when applied for measurement of pores above 50 nm. X-ray computed tomography suffers from resolution limit and the pores below 10 μm are difficult to detect. Applications of the ^{1}H nuclear magnetic resonance relaxometry may become complicated in cementitious materials by considering the naturally large amounts of paramagnetic impurities (such as iron and manganese) and differently bound water fractions.

In most cases the pore structures derived from mercury intrusion porosimetry (MIP) are generally more widely used than those based on other methods. One important reason can be ascribed to the fact that MIP technique is capable of identifying a broad pore size range within few hours' test duration and the results are produced with high reproducibility. Ritter and Drake [14,15] were the first who developed apparatus and methods, as referred to by Zwietering and Koks [16], for

* Corresponding authors.
E-mail addresses: zxyang@fzu.edu.cn (Z. Yang), g.ye@tudelft.nl (G. Ye).

https://doi.org/10.1016/j.cemconres.2022.106942
Received 22 May 2022; Received in revised form 16 July 2022; Accepted 10 August 2022
Available online 17 August 2022

detecting mercury intrusion into chemical substances with pores as low as 20 nm. Since then this technique has been intensively applied to investigate the pore structure of porous systems [17–22]. The relatively high surface tension of non-wetting mercury opposes its entry into pores of the solid. Application of pressure will overcome this opposition and mercury is forced to enter the pores. The pressure required is dependent on the pore geometry and surface properties of the mercury and the solid. The principle of mercury porosimetry relating pressure to pore size was first established by Washburn [23]. With the assumption that pores are cylindrical and entirely and equally accessible to mercury, the correlation between applied pressure and pore diameter can be described using the Washburn equation.

$$d = -4\gamma\cos\theta/P \tag{1}$$

where d is the equivalent pore diameter (μm), P is the pressure required to overcome the opposition to entry (MPa), γ is the surface tension of mercury (0.48 N/m), θ is the contact angle between mercury and pore wall (degree). It should be noted that MIP only measures the open pores that have some interconnections with the exterior porous body.

Standard MIP measurement is very useful to provide estimates of pore structure parameters such as total porosity and threshold diameter. Cementitious capillary pores are composed of long percolating chains, along which there are constrictions, namely choke points. The diameter of these choke points is noted as threshold diameter. On the other hand, MIP has been proved to be inappropriate for measuring the realistic pore size distributions in cementitious materials [19]. Pore size results from MIP are often biased in favor of small pore sizes because it measures pore size on the basis of diameter of accessible throat pores through which mercury penetrates into the microstructure. MIP misinterprets the real pore size distribution, but rather indicates the size distribution of accessible pores.

The accessibility issue [19], also known as ink-bottle effect [9,24,25], is a significant impediment for MIP to reliably gain the pore size distribution of cementitious materials. From the perspective of connectivity of pores in cementitious materials, dead-end and continuous ink-bottle pores have been distinguished in literature [25]. In standard MIP tests, the *pressurization* procedure forces mercury to intrude a pore system through throat pores to reach interior ink-bottle pores [26–30]. In the subsequent *depressurization* procedure, mercury in the throat pores can be freely extruded out while mercury in the interior ink-bottle pores is irreversibly entrapped [19]. Fig. 1 shows schematic illustrations on the mercury entrapment in the ink-bottle pores of an arbitrary porous network after standard MIP test. For the sake of simplicity and clarity, only continuous type of ink-bottle pores is shown in the sense that dead-end type of ink-bottle pores should share the same mechanism of mercury entrapment as described in Fig. 1. Comprehensive spatial data of the ink-bottle pores at various scales of microstructure are particularly important to deeply understand the pore connectivity in cementitious materials. Effective improvements on MIP are therefore a prerequisite to acquire truthful pore size distribution.

The present work describes a novel method called intrusion-extrusion cyclic mercury porosimetry (IEC-MIP), which comprises a number of intrusion-extrusion cycles. The intrusion procedures are conducted by increasing the pressure step-by-step until the maximum pressure is attained. Each intrusion procedure is followed with an extrusion procedure by decreasing the pressure always back to the starting pressure. The IEC-MIP measurement enables to reliably probe the distribution of ink-bottle pores and, together with the microstructure-based mercury penetration model, provides a trustworthy result of the pore size distribution in cementitious materials. A major difference between IEC-MIP and previous methods can be ascribed to the operation of extrusion procedures. Riverberi et al. [27] and Zhou et al. [30], among others, carried out retraction-repenetration measurements while each retraction branch was operated by decreasing the pressure merely to a preset value. More details and advantages of the IEC-MIP method, as well as previous progress in MIP measurements, will be elaborated in the following sections.

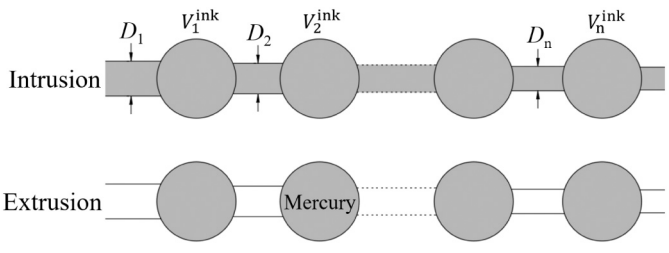

Fig. 1. Mercury entrapment in large (ink-bottle) pores after standard MIP tests. D_1, D_2 and D_n represent the diameter of throat pores; V_1^{ink}, V_2^{ink} and V_n^{ink} represent the volume of ink-bottle pores.

2. Previous research on ink-bottle pores characterization

Significant efforts and many noteworthy contributions have been made on improving mercury porosimetry technique in order to eliminate or minimize the impact of accessibility problem. It is generally assumed that the ink-bottle pores remain filled with mercury after the first mercury intrusion-extrusion cycle while little remaining mercury is expected when performing the second cycle [19,24]. Various techniques including X-ray computed tomography and nitrogen sorption have been utilized, in combination with MIP tests, to explore the ink-bottle effect as well as mercury entrapment in cementitious materials [28,29]. However, a complete distribution of the ink-bottle pores in the entire pore size range can hardly be provided because of measurement limitation of these techniques. Kaufmann et al. [29] applied multi-cycle MIP measurements, whereby the throat pore size distribution and total ink-bottle volume were derived. A large hysteresis was observed between intrusion and extrusion branch in the first cycle. While the following second cycle shows no mercury entrapment, and its extrusion branch is nearly the same as in the first cycle. In the earlier work of Riverberi et al. [27], the ascending branch was measured as usual while the descending branch was operated with a number of steps. For each step, the pressure was decreased always from the maximum pressure to a preassigned value and then increased again to the maximum. The throat pores and ink-bottle volumes were analyzed based on the differences between ascending and descending branches. Analysis of the pore sizes within the ink-bottle volumes was still a pending issue. Mercury retraction starting always from the maximum pressure may result in temperature change, another point worthwhile to be carefully accounted for.

A typically important progress can be referred to the work of Zhou et al. [30], who developed an alternative approach, i.e. pressurization-depressurization cycling mercury intrusion porosimetry (PDC-MIP). The PDC-MIP test comprises a number of pressurization-depressurization cycles. In the nth cycle, the pressure is first increased to P_n^{in} and then decreased to P_n^{ex}. The intruded and extruded mercury volume are recorded as V_n^{in} and V_n^{ex}, respectively. Both pressures P_n^{in} and P_n^{ex} correspond to the same pore diameter D_n by following the Washburn equation with advancing contact angle θ_a and receding contact angle θ_r, respectively, as indicated in Eq. (2).

$$D_n = -\frac{4\gamma cos\theta_a}{P_n^{in}} = -\frac{4\gamma cos\theta_r}{P_n^{ex}} \tag{2}$$

Mercury intrusion-extrusion measurements were carried out on cement pastes with an artificial hole of the known diameter. The pressures forcing mercury to intrude into and extrude from the artificial hole were recorded. The contact angles upon intrusion and extrusion were then calculated using Eq. (2). For cement pastes cured from 1 day to 28 days, the advancing contact angle θ_a increases from 125.4° to 138.0° and the receding contact angle θ_r increases from 118.8° to 128.0° [30]. It is noteworthy that the contact angle can be affected by the temperature and the pore size. Requirements of trustworthy values of both advancing

and receding contact angles impose great challenges for widespread applications of the PDC-MIP method.

The throat pores (diameter D_n, volume V_n^{th}) and interior ink-bottle pores (volume V_n^{ink}) are determined as follows [30]:

$$V_n^{th} = V_n^{ex} \tag{3a}$$

$$V_n^{ink} = V_n^{in} - V_n^{ex} \tag{3b}$$

In the PDC-MIP approach, the pore size distribution of the specimen is analyzed based on an *assumption*: the size distribution of the ink-bottle pores (volume V_n^{ink}) is equal to that of the pores with the diameter larger than D_n, i.e. from D_1 to D_{n-1}. Compared to standard MIP tests, the PDC-MIP tests have been shown to provide better estimates of the pore size distribution in ordinary Portland cement (OPC) pastes with ages of 1–28 days [30].

However, the capability of the PDC-MIP approach in obtaining accurate pore size distribution is not completely assured. As addressed below, the PDC-MIP measurements cannot precisely capture the ink-bottle effect and tend to greatly overestimate the mercury entrapment. This is caused by misinterpretation of the volume ΔV_n of throat pores, which stay filled with mercury after the pressurization-depressurization cycle. In the PDC-MIP tests [30], one hundred pressurization-depressurization cycles (corresponding to throat pore diameters D_n, n = 1– 100) were adopted. The cumulative pore volume as a function of pressure from the PDC-MIP tests of OPC paste specimens with water-cement (w/c) ratio of 0.4, as an example, is provided in Fig. 2.

An important issue that affects the accuracy of pore size results concerns the deficiency of the pressurization-depressurization concept when applied for capturing ink-bottle pores. For each pressurization-depressurization cycle, a number of throat pores are misinterpreted, as illustrated in Fig. 3. It is noted that the cementitious pore structure is rather complicated and the pore network provided in Fig. 3 is a simplified system accounting for continuous pore size distribution and ink-bottle connections between small pores and large pores.

In the nth pressurization, the throat pores (volume V_n^{th}) and interior ink-bottle pores (volume V_n^{ink}) are intruded with mercury. The volume of the throat pores, V_n^{th}, consists of two parts: volume ΔV_n (for pores $D_{n-1} > D > D_n$) and volume ΔV_n^{th} (for pores $D = D_n$). The intruded volume V_n^{in} is then expressed by Eq. (4a):

$$V_n^{in} = V_n^{th} + V_n^{ink} = \Delta V_n + \Delta V_n^{th} + V_n^{ink} \tag{4a}$$

In the nth depressurization, *only* the mercury in throat pores with the specific diameter D_n is extruded out while the remaining throat pores (with diameters $D_{n-1} > D > D_n$, volume ΔV_n) stay filled with mercury. The extruded volume V_n^{ex} is then expressed by Eq. (4b):

$$V_n^{ex} = \Delta V_n^{th} \tag{4b}$$

Eqs. (4a)–(4b) can be rewritten as Eqs. (5a)–(5b):

$$V_n^{th} = V_n^{ex} + \Delta V_n \tag{5a}$$

$$V_n^{ink} = V_n^{in} - V_n^{ex} - \Delta V_n \tag{5b}$$

Disagreements arise between Eqs. (5a)–(5b) and Eqs. (3a)–(3b). The PDC-MIP measurement, namely Eqs. (3a)–(3b), has two consequences:

- The volume of throat pores, V_n^{th}, is underestimated and mistakenly recorded as $(V_n^{th} - \Delta V_n)$.
- The volume of ink-bottle pores, V_n^{ink}, is overestimated and mistakenly recorded as $(V_n^{ink} + \Delta V_n)$.

Similarly, in the $(n + 1)$th pressurization-depressurization cycle, the volume ΔV_{n+1} (representing the volume of throat pores $D_n > D > D_{n+1}$) will also be misinterpreted, as illustrated in Fig. 3.

According to the work of Zhou et al. (i.e. Fig. 7 in Ref. [30]), the cumulative volume of ink-bottle pores, $\sum(V_n^{ink} + \Delta V_n)$, is as high as 90 % of the total pore volume $\sum V_n^{in}$ in the cement paste (w/c = 0.4, 28 days), as expressed in Eq. (6a):

$$\sum_{n=1}^{100}\left(V_n^{ink} + \Delta V_n\right) = 90\% \sum_{n=1}^{100} V_n^{in} \tag{6a}$$

However, as indicated in Fig. 4, mercury hysteresis between intrusion and extrusion from the standard MIP test reveals that the cumulative volume of ink-bottle pores, $\sum V_n^{ink}$, accounts for approximately 45 % of the total pore volume $\sum V_n^{in}$. This, for the sake of comparison, can be expressed as Eq. (6b):

$$\sum_{n=1}^{100} V_n^{ink} = 45\% \sum_{n=1}^{100} V_n^{in} \tag{6b}$$

Substituting Eq. (4a) into Eq. (6a) results in the expression for $\sum \Delta V_n^{th}$:

$$\sum_{n=1}^{100} \Delta V_n^{th} = 10\% \sum_{n=1}^{100} V_n^{in} \tag{7}$$

Substituting Eq. (6b) into Eq. (6a) gives:

$$\sum_{n=1}^{100} \Delta V_n = 45\% \sum_{n=1}^{100} V_n^{in} \tag{8}$$

A comparison between Eq. (8) and Eq. (7) shows that $\sum \Delta V_n$ is much higher (4.5 times) than $\sum \Delta V_n^{th}$. Misinterpretation of the volume ΔV_n in the PDC-MIP measurements can therefore have a great influence on the obtained pore size distribution, i.e. it will generally result in an underestimation of small (throat) pores. In consequence of these observations, it would seem that a truthful pore size determination calls for the needs to proceed with a further improvement to precisely clarify the ink-bottle effect during mercury penetration.

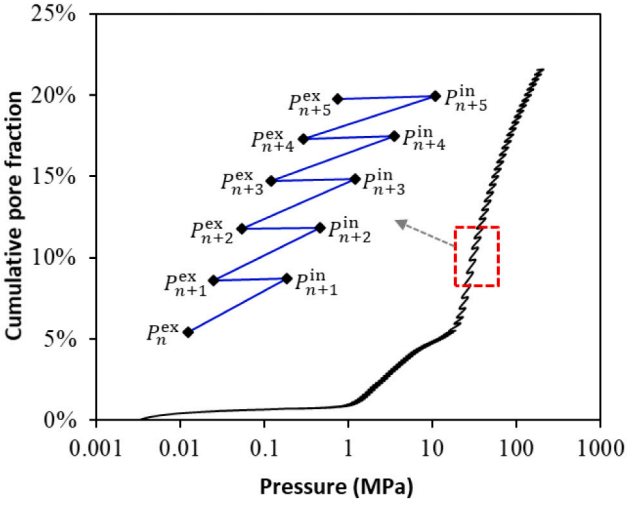

Fig. 2. An example of the PDC-MIP test sequence for analysis of throat and ink-bottle pores in OPC paste specimen (w/c = 0.4, 28 days).

3. IEC-MIP approach

Herein an improved measurement, i.e. intrusion-extrusion cyclic mercury porosimetry (IEC-MIP), is described in order to reliably capture the ink-bottle effect. The principles and test sequence are illustrated in the following.

IEC-MIP consists of a low pressure run from 0 to P_0 and step-by-step high pressure runs. The low pressure run is carried out in the same manner as that of standard MIP tests. After the low pressure run the specimen should be tightly surrounded by the mercury. For the high pressure runs of IEC-MIP tests, the first entire pressurization is divided

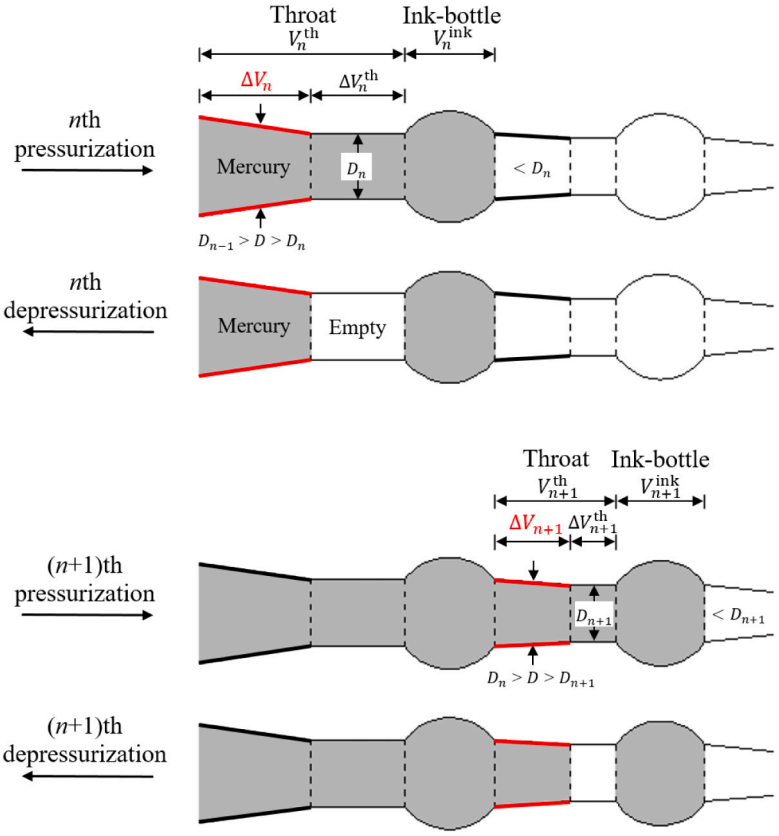

Fig. 3. Schematic representations of pressurization-depressurization from the nth to (n + 1)th cycle in the PDC-MIP measurement.

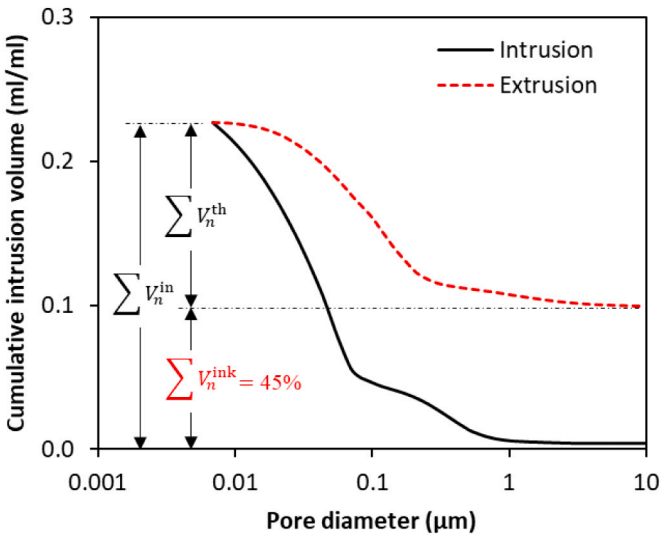

Fig. 4. The total ink-bottle pore volume of 28-day OPC paste (w/c = 0.4) indicated by standard MIP.

into a number of steps ($i = 1, 2…n$). Each high pressure step i contains an intrusion procedure (from P_0 to P_i) and an extrusion procedure (from P_i to P_0). The pressure P_i forces the mercury to intrude pores with the diameter d_i by following the Washburn equation. Fig. 5 illustrates the IEC-MIP test sequence.

At step 1, the pressure is first increased from the minimum P_0 up to P_1, by which the throat pores (diameter d_1 and volume V_1^{th}) and their neighboring ink-bottle pores (volume V_1^{ink}) are filled with mercury. The pressure is then decreased from P_1 down to the minimum P_0, by which mercury in the throat pores d_1 is freely removed while mercury in the ink-bottle pores is entrapped.

At step (i-1), the pressure is first increased from P_0 to P_{i-1}, by which the throat pores (diameters d_1, d_2……d_{i-1}, volumes V_1^{th}, V_2^{th}……V_{i-1}^{th}) and the ink-bottle pores (volumes V_1^{ink}, V_2^{ink}……V_{i-1}^{ink}) are filled with mercury. The pressure is then decreased from P_{i-1} to P_0, by which mercury in the throat pores (diameters d_1, d_2……d_{i-1}) is removed while mercury in the ink-bottle pores (volumes V_1^{ink}, V_2^{ink}……V_{i-1}^{ink}) is entrapped.

At step i, the pressure is first increased from P_0 to P_i, by which the throat pores (diameters d_1, d_2……d_{i-1}, d_i, volumes V_1^{th}, V_2^{th}……V_{i-1}^{th}, V_i^{th}) are filled with mercury. With the ink-bottle pores (volumes V_1^{ink}, V_2^{ink}……V_{i-1}^{ink}) being mercury-filled, the ink-bottle pores (volume V_i^{ink}) connected with the throat pores d_i are further intruded with mercury. In the subsequent extrusion procedure from P_i to P_0, all throat pores are empty while the ink-bottle pores (volumes V_1^{ink}, V_2^{ink}……V_{i-1}^{ink}, V_i^{ink}) are mercury-filled.

At step n, the pressure is increased from the P_0 to the maximum P_n. All throat pores and ink-bottle pores are filled with mercury. In the subsequent extrusion procedure, all throat pores are empty while all ink-bottle pores remain mercury-filled.

Following the IEC-MIP test sequence, the mercury intrudes a pore system through throat pores to reach interior ink-bottle pores. The ink-bottle pores remain filled with mercury after the mercury intrusion and extrusion cycle. From step (i-1) to step i, the cumulative intruded volume increases by ($V_i^{cin} - V_{i-1}^{cin}$) and the cumulative ink-bottle volume increases by ($V_i^{cink} - V_{i-1}^{cink}$), as indicated in Fig. 5b. When mercury penetrates the throat pores of a specific diameter d_i, the volume V_i^{th} of the throat pores and the volume V_i^{ink} of their neighboring ink-bottle pores, as well as the pore entrapment $\alpha_{en,\,i}$, are expressed by Eqs. (9a), (9b) and (9c), respectively.

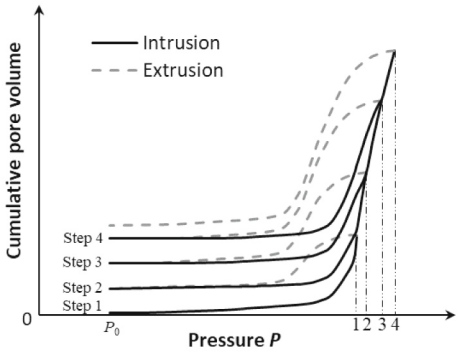

(a) IEC-MIP test sequence with repeated intrusion-extrusion cycles.

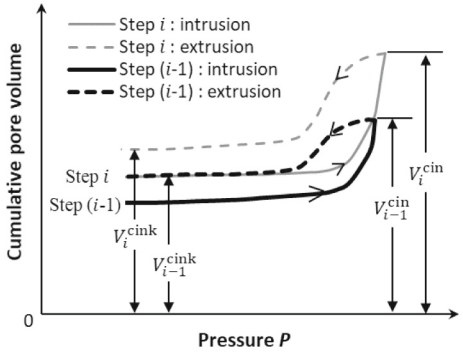

(b) From step (i-1) to step i, the cumulative intruded volume increases from V_{i-1}^{cin} to V_i^{cin} and the cumulative ink-bottle volume increases from V_{i-1}^{cink} to V_i^{cink}

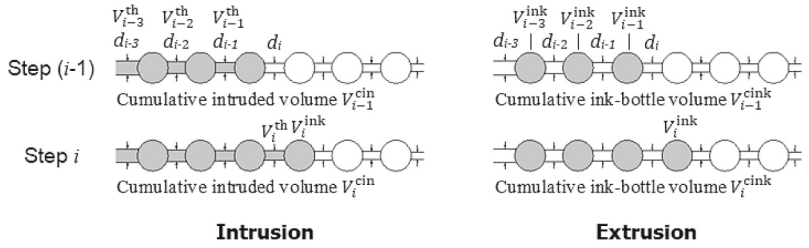

(c) Schematic representations of the mercury intrusion-extrusion in a pore system from step (i-1) to step i.

Fig. 5. Illustration of intrusion-extrusion cyclic mercury porosimetry (IEC-MIP) measurement.

$$V_i^{th} = \left(V_i^{cin} - V_{i-1}^{cin}\right) - \left(V_i^{cink} - V_{i-1}^{cink}\right) \tag{9a}$$

$$V_i^{ink} = V_i^{cink} - V_{i-1}^{cink} \tag{9b}$$

$$\alpha_{en,i} = V_i^{ink} / \left(V_i^{th} + V_i^{ink}\right) \tag{9c}$$

An increase of the number of the total steps enables to obtain a more detailed picture of the ink-bottle pore geometry in the porous system. Compared to PDC-MIP measurements, the IEC-MIP measurements have two *advantages*. First, the contact angles for both intrusion and extrusion are no longer required for IEC-MIP measurements to capture the ink-bottle effect. It is worth noting that accurate determinations of the advancing and receding contact angles are not easy, especially considering that the contact angle can be dependent on the pore size when mercury penetrates the very small pores. Second, the IEC-MIP measurements enable to avoid the misinterpretation of the volume ΔV_n of throat pores as indicated in Fig. 3. The mercury in throat pores can be completely removed for each extrusion step by decreasing the pressure from P_i back to P_0, and this testing sequence allows reliably capturing the throat pore volume V_i^{th} and the ink-bottle pore volume V_i^{ink} at each intrusion-extrusion step i.

4. Experimental

4.1. Materials and specimens

The raw materials used for binder components were OPC (CEM I 42.5 N), ground granulated blast furnace slag (BFS), fly ash (FA) and limestone powder (LP). The particle size distribution of the raw materials as determined by laser diffractometry is presented in Fig. 6. The chemical compositions of the raw materials as measured by X-ray

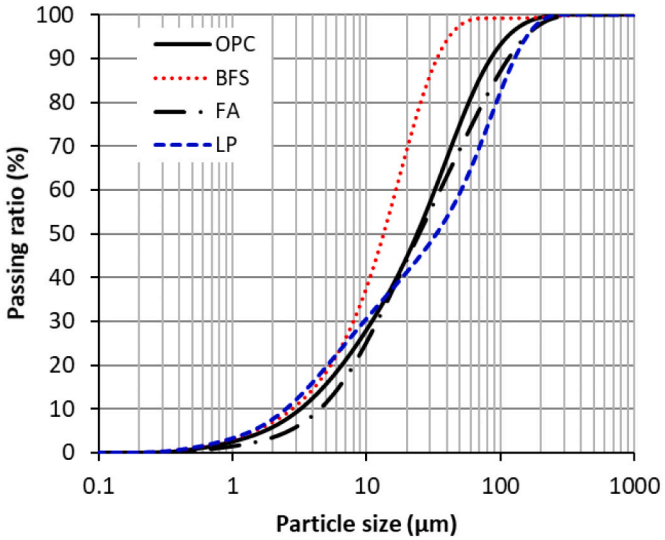

Fig. 6. Particle size distributions of various powders by laser diffractometry.

fluorescence are provided in Table 1.

OPC and blended paste specimens were prepared for IEC-MIP tests. The blended mixtures were fabricated with often-adopted replacement levels of 30 % FA, 70 % BFS and 5 % LP by mass of the binder. The water-binder (w/b) ratio varied from 0.4 to 0.6. Table 2 gives the detailed mixture proportions of the paste specimens. The raw materials and deionized water were mixed at low speed for 1 min and at high speed for another 2 min. Immediately after mixing the fresh pastes were poured into small plastic bottles. The bottles were carefully vibrated to remove big air bubbles while preventing any segregation and then sealed with lids. Rotation of the paste-filled bottles was carried out for 24 h in order to prevent bleeding. The bottles were then moved to a fog room maintaining a constant temperature at 20 ± 0.1 °C. At the age of 28, 105, 182 and 370 days, the paste specimens were taken out of the bottles and crushed into small pieces (around 1 cm^3). The pieces smaller than 3 mm were not used to avoid additional intrusion of mercury caused by interparticle void [31]. Freeze-drying method [25], owing to the slightest damage on the specimen, was adopted to stop hydration and remove the pore water from the paste pieces. The paste pieces were soaked in liquid nitrogen at −195 °C and left to rest for 5 min. The paste pieces were then moved to a freeze-drier maintaining at −24 °C and 0.1 Pa until a constant mass was reached. Freezing the specimens at very low temperature enabled to produce ice microcrystals and avoided the growth of big ice crystals that may create compressive stresses in the small pores.

4.2. IEC-MIP measurements

The paste pieces after freeze-drying procedure were carried out with IEC-MIP tests using Micromeritics PoreSizer 9320, which has a capacity of 210 MPa. Note that there is a slight compressibility for mercury when compressed at pressure around 20 MPa. At very high pressures, thermo expansion may occur and alter the volume of mercury intruded into the specimen. Given these systematic errors, a blank experiment was performed with IEC-MIP measurement using empty penetrometer. The blank test was used for volume correction due to mercury compression and heating/cooling during measurement.

In this work the IEC-MIP tests started with a low pressure run from 0 to P_0 (0.15 MPa), followed by high pressure runs with 20 intrusion-extrusion steps. The details of the high pressure runs including the maximum applied pressure P_i and minimum intruded pore diameter d_i at each step i are listed in Table 3. As indicated, the first entire pressurization is divided into 19 steps. The intrusion step 20 represents the second pressurization of MIP. The P_i values were given based on statistical analysis of a considerable number of mercury porosimetry data. A variety of pore structure parameters were figured out. The critical pore diameter d_{cr} and threshold pore diameter d_{th} were determined by differential curves of cumulative intruded mercury vs. pore diameter derived from intrusion step 20 as shown in Table 3. Analysis and calculation of the pore size distribution will be presented more in detail in the Discussion part. The ultimate mercury entrapment α in the entire pore structure represents the overall hysteresis between intrusion and extrusion steps, as calculated in Eq. (10), where $\sum V_i^{ink}$ and $\sum V_i^{th}$ represent the ink-bottle porosity and effective porosity, respectively. The pore connectivity η can be described as the ratio of effective porosity over total porosity, as seen in Eq. (11). The CPSM model from Salmas and Androutsopoulos [32] as shown in Eq. (12) was used to evaluate the pore tortuosity τ of the porous cementitious systems.

$$\alpha = \frac{\sum V_i^{ink}}{\sum V_i^{ink} + \sum V_i^{th}} \tag{10}$$

$$\eta = \frac{\sum V_i^{th}}{\sum V_i^{ink} + \sum V_i^{th}} = 1 - \alpha \tag{11}$$

$$\tau = 4.6242 ln\left[\frac{4.996}{1-\alpha} - 1\right] - 5.8032 \tag{12}$$

4.3. Thermogravimetric analysis

Thermogravimetric analysis (TGA) was performed to monitor thermal decompositions of the cementitious hydrates with elevated temperature. The freeze-dried paste pieces were milled into powders (<50 μm). The dry powders of around 30– 50 mg were placed in a corundum crucible that was supported by a precision balance. The weight loss was recorded from ambient temperature to the maximum 1000 °C with a heating rate 10 °C/min in STA(TG-DTA-DSC) 449 F3 Jupiter. Argon was used as the protective gas to control the sample environment. The deviation of the TG signal, namely DTG curve, was adopted to characterize the phase changes as a function of temperature. Meanwhile the hydrate assemblage can be distinguished between different mixtures.

Table 1
Chemical composition of the raw materials (g/100 g).

Item	OPC	FA	BFS	LP
CaO	64.495	5.537	41.398	–
SiO_2	18.875	50.554	34.015	0.737
Al_2O_3	4.481	30.743	11.117	0.180
Fe_2O_3	3.686	6.301	0.529	0.073
MgO	2.012	1.009	8.284	0.523
K_2O	0.508	1.109	0.398	0.026
Na_2O	0.341	0.284	0.205	0.010
SO_3	2.625	0.785	2.430	0.082
TiO_2	0.319	2.362	1.027	0.020
$CaCO_3$	1.185	–	–	98.316
Others	3.824	1.316	0.597	0.033
LOI	3.04	2.66	0.38	43.26
Specific gravity (g/cm^3)	3.12	2.26	2.87	3.08

Table 2
Mixtures for the paste specimens.

Binders	Raw materials and replacement (weight percentage)				w/b
	OPC	FA	BFS	LP	
P4	100 %	–	–	–	0.4
P5	100 %	–	–	–	0.5
P6	100 %	–	–	–	0.6
PF5	70 %	30 %	–	–	0.5
PFL5	65 %	30 %	–	5 %	0.5
PB5	30 %	–	70 %	–	0.5
PBL5	25 %	–	70 %	5 %	0.5

Table 3
The applied pressure increases from P_0 (0.15 MPa, $d_0 = 10$ μm) to P_i (d_i) and then decreases from P_i to P_0 at each intrusion-extrusion step i (i = 1– 20) in the high pressure runs of IEC-MIP tests (contact angle $\theta_a = 138°$ for intrusion). The first entire pressurization is divided into 19 steps. The intrusion step 20 represents the second pressurization of MIP.

Steps i	P_i [MPa] (d_i [nm])	Steps i	P_i [MPa] (d_i [nm])
1	3.4 (422.7)	11	77.7 (18.6)
2	5.6 (259.2)	12	95.7 (15.1)
3	10.4 (138.6)	13	109.9 (13.1)
4	15.8 (91.1)	14	117.8 (12.2)
5	20.8 (69.4)	15	126.3 (11.4)
6	25.6 (56.4)	16	135.4 (10.6)
7	31.5 (45.8)	17	166.8 (8.6)
8	33.9 (42.6)	18	178.7 (8.1)
9	41.6 (34.6)	19	210.0 (6.9)
10	58.9 (24.5)	20	210.0 (6.9)

5. Results

5.1. Data analysis of IEC-MIP test sequence

Table 4 summarizes the results of cumulative intruded volumes V_i^{cin} at steps 5, 10 and 19 based on IEC-MIP tests of five replicates of OPC paste (w/c = 0.4, 28 days). The differences between the maximum and minimum intruded volumes are 0.0019, 0.0090 and 0.0169 ml/ml for V_5^{cin}, V_{10}^{cin} and V_{19}^{cin}, respectively. For any particular step i (i = 1– 20), the difference of the intruded volumes V_i^{cin} is within ±3 %. The difference of the total porosities ϕ_t is within ±5 %. The IEC-MIP shows a high reproducibility in view of pore volume measurements.

Fig. 7a presents an example of the cumulative pore volume obtained from IEC-MIP tests of OPC paste specimens (w/c = 0.5, one year) by following Table 3. In order to show the result more clearly, Fig. 7b plots the mercury intrusion-extrusion at the applied pressure of 33.9– 95.7 MPa, corresponding to steps 8– 12. As can be seen, the higher applied pressure leads to higher cumulative intrusion volume. An intrusion-extrusion step i (i = 1– 19) always shows a hysteresis, indicating that the ink-bottle effect exists in the entire pore size range. The hysteresis, however, depends on the applied pressure and can be divided into three stages.

1) In the first stage (steps 1– 4), mercury intrudes the surface of the specimen. Only a minor intrusion volume is detected. This part of mercury intrusion is often not of interest. Some uncertainties caused by factors including insufficient penetration and air bubbles lying on the specimen surface may affect the intruded volume of mercury.
2) In the second stage (steps 5– 9), the intruded volume increases abruptly when the threshold pores (diameter d_{th}) are filled with mercury. Plenty of mercury is intruded within a narrow pore size range of 34.6– 69.4 nm, but most of the intruded mercury is irreversibly entrapped. Obviously, strong ink-bottle effect presents and the intruded pores are poorly connected.
3) In the third stage (steps 10– 20), after the critical pores (diameter d_{cr}) are filled with mercury, a considerable amount of mercury continues to intrude the small pores. The majority of the intruded mercury is removable after the extrusion step. It is considered, therefore, that weak ink-bottle effect presents and these small pores are highly interconnected.

In the present study, the initial volume of mercury extruded at step i was always filled at the next intrusion step (i + 1) and a closed loop was then formed after the extrusion-intrusion procedure. Occasionally a small discrepancy within 3 % occurred at the high pressures, implying that damage to the specimens during the measurement was insignificant. The small discrepancy was found at around 30 MPa (pore diameter 50 nm) for both OPC pastes and FA-blended pastes, while it was at 70 MPa (pore diameter 20 nm) for BFS-blended pastes.

Fig. 8 shows the ink-bottle effect characterized by different measurements performed on 28-day OPC paste specimens. Standard MIP is considered inappropriate for analyzing the pore size distribution but it is justified to quantify the total volume of ink-bottle pores, noted as ink-bottle porosity ϕ_{ink} and equal to the volume difference between pressurization and depressurization. For both IEC-MIP and PDC-MIP measurements, the cumulative ink-bottle volume increases with smaller diameter of the pores intruded, an expected observation. At the smallest intrusion pore diameter the cumulative ink-bottle volume V_i^{cink} obtained from IEC-MIP is consistent with the ink-bottle porosity ϕ_{ink} from standard MIP, while both are much smaller than the cumulative ink-bottle volume V_p^{cink} from PDC-MIP. Reliability of the IEC-MIP measurement for the ink-bottle pores determination can thus be confirmed.

Table 4
Cumulative intruded volumes V_i^{cin} (ml/ml) at steps 5, 10 and 19 based on IEC-MIP tests of five replicates of OPC paste (w/c = 0.4, 28 days).

Sample no.	Weight (g)	V_5^{cin}	V_{10}^{cin}	V_{19}^{cin}
1	4.3592	0.0404	0.1506	0.2191
2	4.5689	0.0423	0.1509	0.2096
3	4.2286	0.0415	0.1565	0.2265
4	4.7325	0.0419	0.1486	0.2237
5	5.0269	0.0421	0.1576	0.2126
Average	4.5832	0.0416	0.1528	0.2183

5.2. Ink-bottle effect and pore entrapment

A high ink-bottle volume does not necessarily ensure a strong ink-bottle effect in case the volume of throat pores is high. The term pore entrapment $\alpha_{en,\,i}$ is adopted to quantitatively describe the ink-bottle effect when mercury intrudes the throat pores of a particular diameter d_i. According to pressure Table 3, the IEC-MIP tests were composed of 20 intrusion-extrusion steps. With increased intrusion step the pore entrapment $\alpha_{en,\,i}$ can be plotted against pore diameter d_i using Eqs. (9a), (9b) and (9c). As shown below, changes of the α_{en} with the pore diameter d varying in the range 0.005– 0.5 μm are given for various cementitious paste specimens.

Fig. 9 shows the distribution of pore entrapment (α_{en}-d plots) for one-year OPC paste specimens of different w/b ratio. All the curves are present in similar pattern and strong α_{en}-d relationships can be seen. Lower w/b ratio tends to result in higher pore entrapment α_{en}. This is true almost in the whole pore size range. The decrease of w/b ratio results in less void space between cement grains after mixing and the hydration front of one cement grain is more likely to contact with adjacent cement grain as hydration proceeds. A lager amount of small (throat) pores, as well as higher α_{en}, can be expected. A common feature is observed that all the α_{en}-d plots of OPC pastes can be divided into two groups corresponding to the pore size d above and below the critical pore diameter d_{cr}, respectively. For $d \geq d_{cr}$, the α_{en}-values are generally high (around 70 %), indicating strong ink-bottle effect. For $d < d_{cr}$, the α_{en}-values are generally low (around 30 %), indicating small ink-bottle effect. In other words, the small pores ($d < d_{cr}$) are highly interconnected. The pore entrapment α_{en} appears to be inherently related to the critical pore size. In this regards a detailed discussion will be presented later on.

Fig. 10 shows the α_{en}-d relations in paste specimens with different binders. For the pores above 0.05 μm the α_{en}-values are normally high and mostly lie in a narrow range 60– 78 %, regardless of the binders. For the small pores the α_{en}-values vary significantly for different binders. Compared with the OPC binder (P5), the binders with 30 % FA or 70 % BFS show much higher α_{en}-values for the pores below 0.035 μm. In particular for the BFS-blended binder PB5 the α_{en} value can reach as high as 80 % at the nanoscale pore size of around 0.01 μm. It can be deduced that adding 30 % FA or 70 % BFS substantially reduces the connectivity of small pores.

The presence of 30 % FA enhances the pore entrapment in the whole pore size range compared to neat OPC paste. Due to the less reactive nature, the unreacted FA particles act like barriers that impair the connections of large pores, resulting in higher α_{en} for large pores. The reacted FA particles consume calcium hydroxide (CH) and produce extra calcium silicate hydrate (C-S-H), resulting in denser packing of hydrates and higher α_{en} for small pores. The addition of BFS has a small influence on the α_{en} for the pores above 0.035 μm while tremendously increases the α_{en} for the pores below 0.035 μm. The significant change of α_{en} due to BFS addition is intimately related to its reactive nature. Besides a fine particle size distribution (Fig. 6), the BFS has strong pozzolanic and latent hydraulic reactivities. The presence of BFS can greatly strengthen the packing density of hydration products, resulting in higher α_{en} for small pores.

It is clear that the dependency of the ink-bottle effect on the throat pore size varies from different binders. For OPC binders the critical pore diameter plays a crucial role, above which the ink-bottle effect is significant while below which the ink-bottle effect is less severe. For

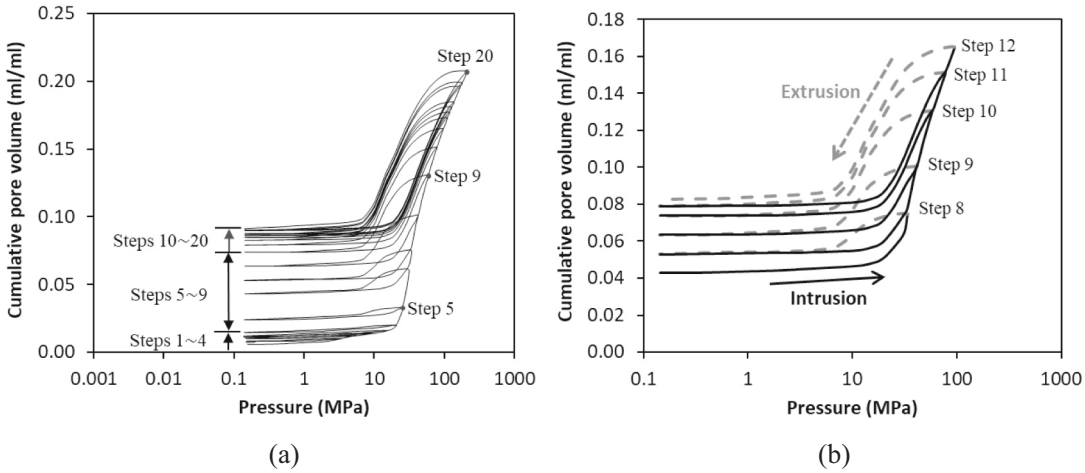

Fig. 7. Cumulative pore volume derived from the IEC-MIP tests of OPC paste (w/c = 0.5, one year).

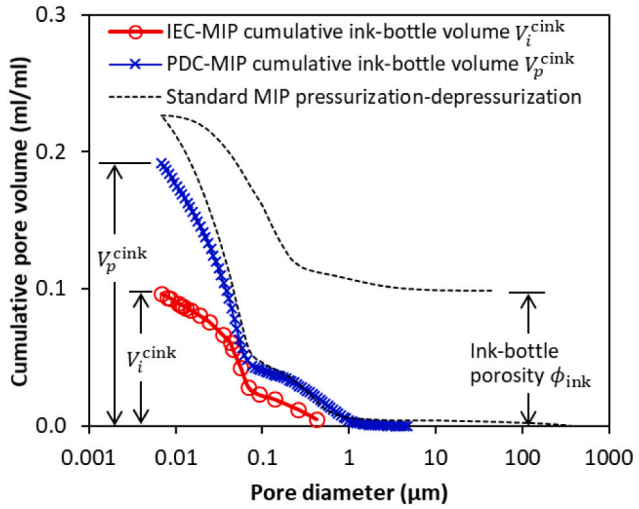

Fig. 8. Cumulative ink-bottle volume obtained from IEC-MIP and PDC-MIP and comparison with the ink-bottle porosity ϕ_{ink} from standard MIP. OPC paste, w/c = 0.4, 28 days.

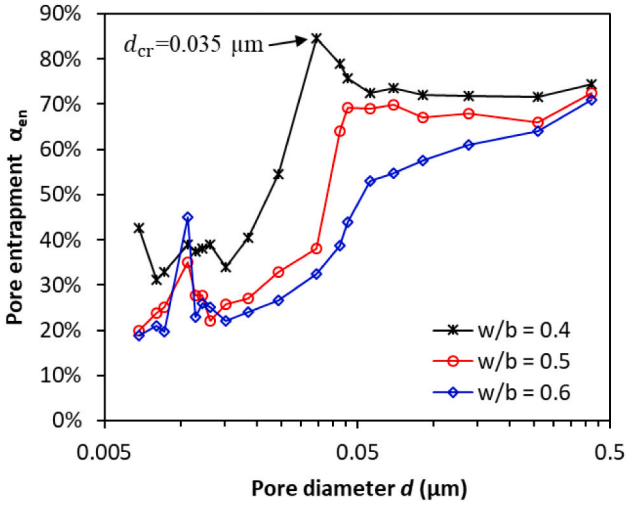

Fig. 9. Effect of w/b ratio on the distribution of pore entrapment obtained from IEC-MIP tests of one-year OPC paste specimens.

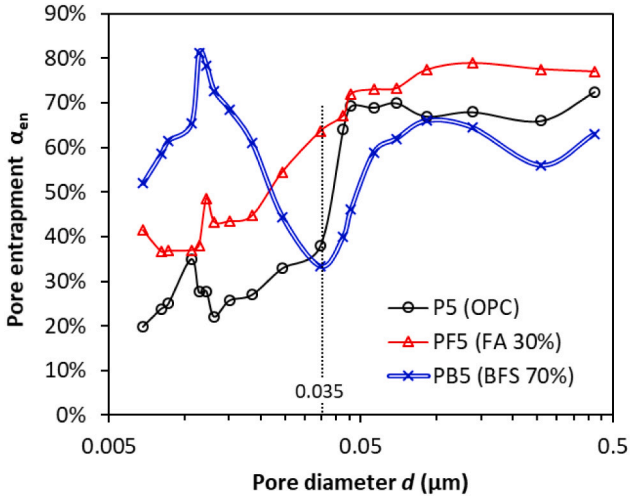

Fig. 10. Effect of binder type on the distribution of pore entrapment (α_{en}-*d*) obtained from IEC-MIP tests of one-year paste specimens (w/b = 0.5).

blended binders, especially when reactive powders are included, the role of critical pore diameter in the connectivity of small pores may become complicated owing to the complexity of hydrates packing by the coexistence of cement hydration and pozzolanic reaction. It should also be borne in mind that the distribution of pore entrapment as a function of throat pore diameter enables a better understanding of the ionic transport in porous systems. This is particularly true for unsaturated porous systems, where the small pores are water-filled facilitating ionic transport and the large pores are only adsorbed with thin film facilitating water movement or gas transport [5]. The IEC-MIP measurements enable to distinguish between throat pores and ink-bottle pores. The connectivity between small pores and large pores can be well described accordingly. Representative results can be deduced from Figs. 9 and 10. A high pore entrapment (large ink-bottle effect) reflects that the small pores are intimately connected with the large pores, while a low pore entrapment (small ink-bottle effect) stands for interconnections of the small pores. It is the highly interconnected (water-filled) small pores that play a dominant role in the unsaturated ionic transport properties.

5.3. Pore connectivity and tortuosity

The dimensions of capillary pores of cementitious materials in general vary from nanometers to micrometers. One capillary pore in-

terconnects with another and overall constituting into a complex pore network. Pore connectivity is regarded as the most common parameter used for mass transport studies. The first attempts in pore connectivity determinations can be referred to the early works reported by Jennings and Johnson [33] and Bentz and Garboczi [34]. Both simulated tricalcium silicate C_3S hydration and described phase percolation under different conditions. Navi and Pignat [35] introduced an integrated particle kinetics model for C_3S hydration accounting for interparticle contacts and built up a single curve between pore connectivity η and total porosity ϕ_t, independent of w/b ratio. It has been common to relate the pore connectivity η to total porosity ϕ_t mainly because of the ease with which the total porosity ϕ_t can be tested. In this work, the experimentally derived η-ϕ_t plots covering a variety of mixtures are provided in Fig. 11. The ϕ_t value varies from 7.8 % to 37.3 % and the η value changes in the range 25.5– 66.1 %, depending on the w/b ratio or the binder. There is a tendency for the pore connectivity η to be increased with higher total porosity ϕ_t. A general η-ϕ_t relationship can be described with Eq. (13).

$$\eta = \phi_t \bullet exp(1-\phi_t) \tag{13}$$

Table 5 shows the results of the pore tortuosity τ of various paste specimens following the CPSM model, see Eq. (12). The τ value is present in the range 2.89–5.81. It is generally increased with a higher age, irrespective of the binders, and decreased with a higher w/b ratio. For OPC binder P5, the pore tortuosity τ exhibits merely a small increase from 3.41 at 28 days to 3.67 at 370 days. For FA-blended binder PF5, in contrast, the τ value increases remarkably from 3.42 to 4.72 by extending the age from 28 up to 370 days, owing to the slow reaction of FA particles. In the presence of reactive BFS, the binder PB5 has the largest pore tortuosity τ and its value is much higher than that of OPC binder P5 even at 28 days. When a small amount of LP (5 %) is included, the binder PBL5 shows significantly lower pore tortuosity τ than the binder PB5 at any age.

5.4. Porosity

The total intruded volume of mercury allows for evaluating the open porosity accessible at the maximum applied pressure. The total open porosity, often noted as total porosity, refers to the cumulative volume at the smallest intrusion pore size. The effective porosity ϕ_e corresponds to the total volume of extruded mercury. The ink-bottle porosity ϕ_{ink} represents the total irreversible mercury entrapment between intrusion and extrusion cycles. In this work, the total porosity ϕ_t of paste specimens was determined as the total intruded volume of mercury at the last intrusion step 20 when the maximum pressure 210 MPa was applied, i.e. $\phi_t = V_{20}^{cin}$. The ink-bottle porosity ϕ_{ink} was equal to the total remaining volume of mercury at the last extrusion step 20 when the applied pressure was decreased from 210 MPa to P_0 (0.15 MPa), i.e. $\phi_{ink} = V_{20}^{cink}$. Determinations of V_{20}^{cin} and V_{20}^{cink} can be referred to the illustrations shown in Fig. 5b. For a specimen with hydration age $t = 0$, the ϕ_t-value, i.e. non-solid phase and no air volume considered, was estimated as:

$$\phi_t(t=0) = \frac{w/b}{\frac{w}{b} + \frac{m_b}{\rho_b} + \frac{m_c}{\rho_c}} \tag{14}$$

where w/b is the water-binder ratio, m_c and m_b are the mass percentage of Portland cement and blended cement, respectively; ρ_c and ρ_b are the specific gravity of Portland cement and blended cement, respectively. For OPC pastes, $m_b = 0$.

Fig. 12 shows the total porosity ϕ_t of OPC pastes with w/b ratios of 0.4, 0.5 and 0.6. In general the total porosity ϕ_t decreases sharply in the first 28 days, followed by a gradual slow decrease. For instance the ϕ_t-value of P4 drops drastically from 55.5 % ($t = 0$) to 21.9 % ($t = 28$ days), compared to 15.4 % at 370 days. The decrease of the ϕ_t-value is attributable to the continuous hydration of cement, which takes place rapidly at early age and proceeds slowly at later age. An increase of the w/b ratio of 0.1 results in an increase of the ϕ_t-value of around 5.4– 7.2 %, depending on the age (28– 370 days). This is intimately related to the larger distance between hydrating cement grains for a higher w/b ratio. A lower w/b ratio or a higher age leads to a significant decrease of the effective porosity ϕ_e (see Fig. 13a). Both w/b ratio and age, however, play only a minor role in the ink-bottle porosity ϕ_{ink} (see Fig. 13b). It is reasonable to assume that the large capillary pores contribute most to the ink-bottle porosity while the effective porosity is constituted by small (throat) pores. The hydration of cement consumes the free water in capillary pores and the remaining capillary water preferentially occupies the small pores. After 28 days the cement hydration and associated precipitation of hydrates tend to occur mainly in the water-filled

Table 5
Pore tortuosity τ of cementitious pastes analyzed based on CPSM model.

Binders	w/b	Pore tortuosity τ with age (days)			
		28	105	182	370
P4	0.4	3.94	4.30	4.50	4.93
P5	0.5	3.41	3.52	3.57	3.67
P6	0.6	2.89	2.94	2.96	3.09
PF5	0.5	3.42	3.88	4.40	4.72
PFL5	0.5	3.23	3.66	3.81	3.84
PB5	0.5	4.91	5.42	5.45	5.81
PBL5	0.5	3.72	3.80	3.86	3.91

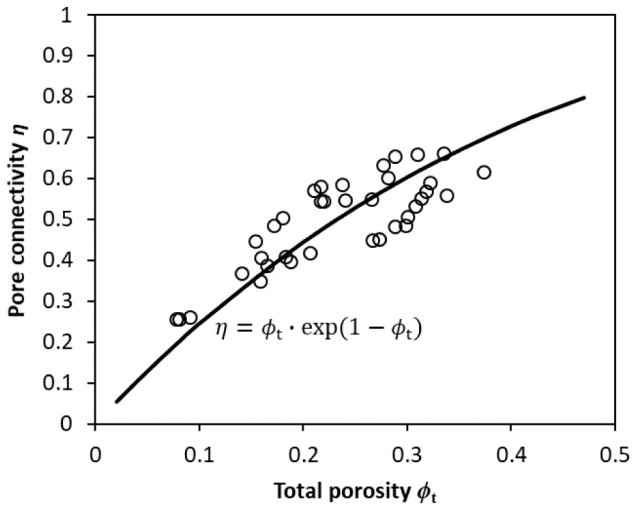

Fig. 11. Evolution of pore connectivity η as a function of total porosity ϕ_t in cementitious pastes.

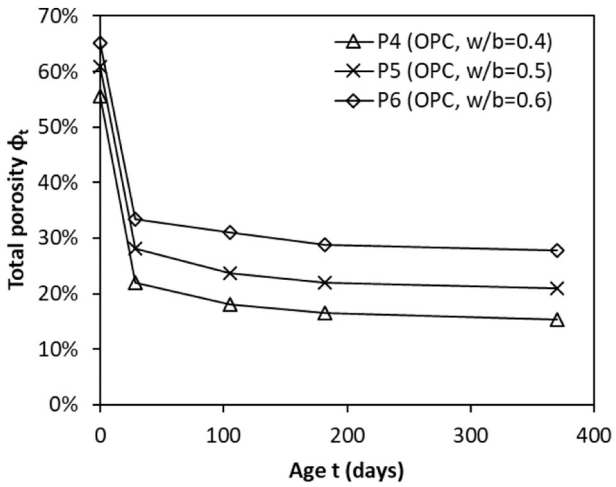

Fig. 12. Evolution of the total porosity of OPC pastes with age.

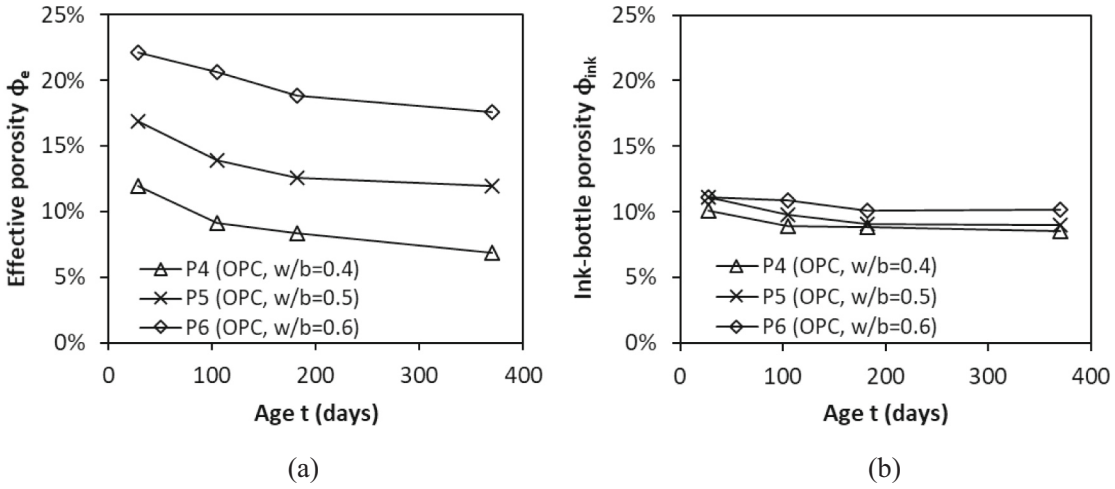

Fig. 13. Effective porosity (a) and ink-bottle porosity (b) in OPC pastes at different ages.

small pores and the volume of small pores is decreased subsequently, i.e. the effective porosity shows a decreasing trend with age. Mehta and Manmohan [36] explained that, at early stage, the hydration products were formed in large capillary pores, whereas later on in small capillary pores.

The effects of blended materials including FA, BFS or LP on the total porosity ϕ_t are shown in Fig. 14. Incorporating 30 % FA (PF5) results in a higher total porosity ϕ_t than that of the reference cement paste (P5) at all ages. This is in agreement with the results reported by Chindaprasirt et al. [37]. Partial replacement of OPC by FA leads to a relatively higher water-cement ratio and lower gel-space ratio, resulting in a higher porosity [38]. The gel-space ratio refers to the quotient of the volume of hydration products over the volume of both hydration products and capillary pores. The porosity increment with FA addition also partly results from the hollow nature of FA particles. These hollow voids can be filled with mercury and contribute to the porosity measured. However, a larger amount of small pores corresponding to the gel pore system is present in the FA-blended paste PF5 than in the OPC paste P5, as reflected by the IEC-MIP tests of one-year specimens. The paste containing 70 % BFS (PB5) shows a lower total porosity ϕ_t than the OPC paste P5 at all ages. This proves a strong chemical reactivity of the BFS owing to its fine particle size and considerable amount of amorphous phases. The ϕ_t-value of PB5 drops sharply in the first 105 days, followed by a slow decline trend thereafter. The total porosity ϕ_t of LP-filled pastes PFL5 (PBL5) is obviously higher than the LP-free pastes PF5 (PB5). Such porosity increase can be ascribed to the dilution effect of LP in the paste systems. The porosity difference is noted as $\Delta\phi_F$ between PFL5 and PF5, and as $\Delta\phi_B$ between PBL5 and PB5. It appears that the $\Delta\phi_B$ values are markedly larger than the $\Delta\phi_F$ values of the same age. In this respect a detailed discussion will be presented in Subsection 6.1.

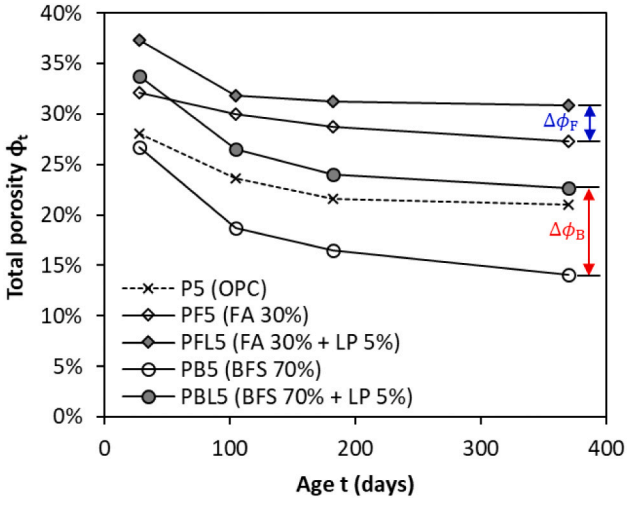

Fig. 14. Effect of blended materials on the total porosity of paste specimens.

The results of total porosity given in Fig. 14 are the summary of effective porosity ϕ_e and ink-bottle porosity ϕ_{ink}. For a further analysis, the ϕ_e and ϕ_{ink} values of various paste mixtures are presented in Fig. 15a and b, respectively. The effective porosity ϕ_e is commonly decreased with a higher age. This observation applies for all binders, as seen in Fig. 15a. Precipitations of the hydration products in the water-filled small pores are responsible for the volume decrease of small (throat) pores after 28 days. The FA-blended binders (PF5 and PFL5) have the largest effective porosity ϕ_e at all ages, indicating an abundant formation of small pores. A larger decrease of the ϕ_e value with age is found in the binders blended with FA or BFS as compared to that in the OPC binder P5. The LP-filled binders PBL5 show a substantially higher effective porosity ϕ_e than the LP-free binders PB5 at all ages. It is true also for FA-blended binders but that a relatively smaller difference of ϕ_e exists between PFL5 and PF5. These observations are consistent with the different roles of LP in the total porosity between BFS and FA blended binders as given in Fig. 14.

The influences of various blended materials on the ink-bottle porosity ϕ_{ink} are quite different from their effects on the effective porosity ϕ_e. As indicated in Fig. 15b, at 28 days the OPC binder P5 shows the smallest ink-bottle porosity ϕ_{ink} compared to the largest ϕ_{ink} in the BFS-blended binders. With ongoing hydration the FA-blended binders (PF5 and PFL5) exhibit merely a minor change of the ϕ_{ink} values, a similar observation for P5. For BFS-blended binders (PB5 and PBL5), in contrast, the small pores are one important part of the ink-bottle porosity ϕ_{ink} and these small pores can be gradually filled with hydrates, as reflected by a decreasing trend of the ϕ_{ink} values. The ink-bottle porosity ϕ_{ink} of blended binders incorporating FA or BFS is commonly higher than that of OPC binder at nearly all ages. The addition of LP plays a minor role in the ink-bottle porosity ϕ_{ink} after comparing the data between PF5 and PFL5. This finding is also applicable between BFS-blended binders PB5 and PBL5. At 370 days the FA-blended binders possess the largest ink-bottle porosity ϕ_{ink}, followed by BFS-blended binders and OPC binders in a descending order. It is noted that the significantly higher ink-bottle porosity ϕ_{ink} of FA-blended binders (PF5 and PFL5) should partially result from the presence of hollow voids within initial boundary of the FA particles. These hollow voids in fact do not represent the originally water-filled spaces between cement grains, the accepted concept of the origin of capillary pores [39].

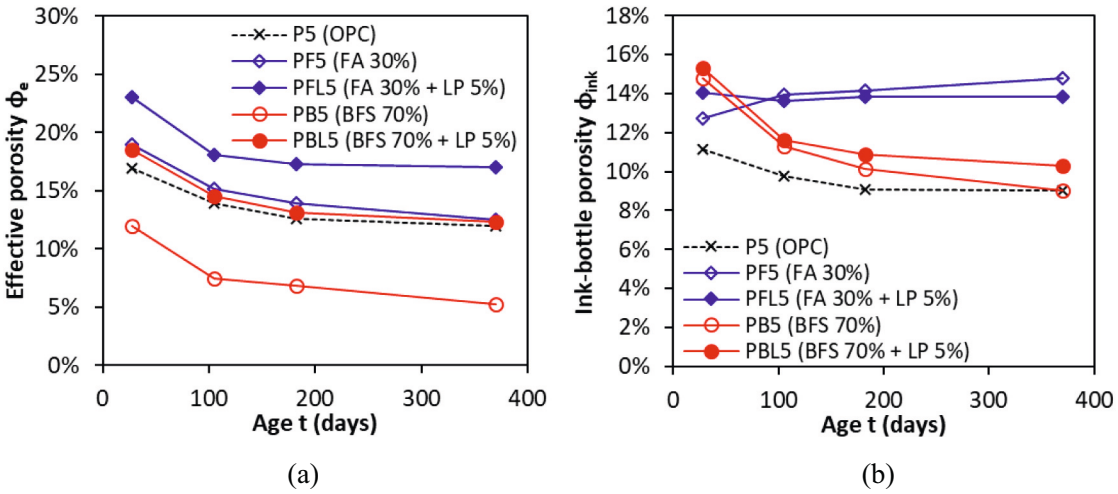

Fig. 15. Effective porosity (a) and ink-bottle porosity (b) in blended paste specimens at various ages.

6. Discussion

6.1. Effect of LP on total porosity

The results shown in Fig. 14 indicate that the $\Delta\phi_F$ values are much smaller than the $\Delta\phi_B$ values at all ages. A synergistic effect is expected when LP is used together with FA. Such synergistic effect promotes the hydration of LP and can be ascribed to the high alumina content of FA grains (30.7 wt%). The presence of alumina-rich FA lowers the sulphate to alumina ratio and, therefore, impairs the transformation of ettringite (AFt) to monosulphate (Ms). The volume of AFt is much higher than that of Ms, i.e. 707 cm^3/mol vs. 309 cm^3/mol at 25 °C [40]. The main component of LP is $CaCO_3$ (CC). Combining FA with LP tends to form the alumina-carbonate compounds, i.e. hemicarboaluminate (Hc) or monocarboaluminate (Mc) [41], as:

$$C_3A + 1/2CH + 1/2\ CC + 11.5H_2O \rightarrow C_3A \bullet 1/2CC \bullet 1/2CH \bullet 11.5H_2O\ (Hc) \quad (I)$$

$$C_3A + CC + 11H_2O \rightarrow C_3A \bullet CC \bullet 11H_2O\ (Mc) \quad (II)$$

Fig. 16 shows the differential thermogravimetric analysis (DTG) curves of one year cementitious pastes with and without LP in the temperature range 50– 250 °C. The first peak starting from 70 °C is related to decomposition of AFt. The mass loss due to dehydroxylation of C-S-H phase, as reported by Lothenbach et al. [42] and Scrivener et al. [43], takes place in a wide temperature range 100– 600 °C and acts as polynomial baseline below other peaks. The peaks above 150 °C correspond to the stepwise dehydration of AFm phases including Hc/Mc and Ms. Considerably higher endothermic peak related to AFt can be observed in the FA-blended systems, particularly when the LP is present, than in the BFS-blended systems. The peaks corresponding to alumina-carbonate hydrates Hc/Mc become pronounced with the addition of LP. The phase changes as observed in Fig. 16 agree well with the findings from De Weerdt et al. [44].

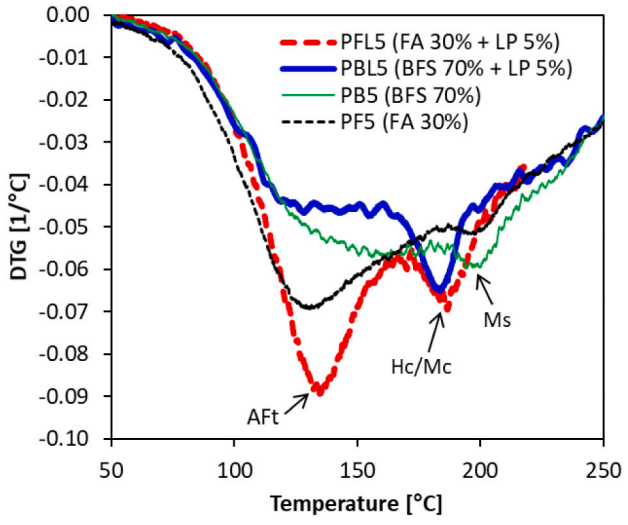

Fig. 16. Differential thermogravimetric analysis (DTG) for blended paste specimens with and without LP (w/b = 0.5, 370 days).

6.2. Role of critical pores in pore entrapment

The distribution of pore entrapment α_{en} of OPC pastes, as seen from Fig. 9, seems to be inherently dependent on the critical pore diameter d_{cr}. It is generally assumed that the mercury can penetrate the bulk specimen once the pressure corresponding to the critical pore diameter d_{cr} is applied. An abrupt decrease of the pore entrapment α_{en} from large pores ($d \geq d_{cr}$) to small pores ($d < d_{cr}$) provides an evidence of a strongly pore size-dependent ink-bottle effect, as discussed below.

Based on the integrated particle kinetic concept from Van Breugel [45] and the work from Jennings [46], all the anhydrous particles are considered to be spherical in shape. The hydrates are preferred to precipitate in the vicinity of the dissolving cement grains. Both the dissolution and growth process of the cement particles are assumed to occur concentrically until particles contact with each other. After contact with water, the cement grains gradually dissolve and porous shells of hydrates are formed around these grain particles. With further hydration, each grain particle grows outward and embeds the neighboring particles. A considerable amount of pore size is formed with the precipitation of hydrates. Based on different refinement mechanisms, the pore family can be categorized into three types: (1) nanoscale gel pores inside inner hydrates, which pack up with high density; (2) small capillary pores formed due to the insufficient packing of hydrates in the outer products layers; (3) large capillary pores representing spaces left out of the outer products layers.

A sketch of cement paste microstructure (Fig. 17) and a typical pore size distribution obtained from standard MIP test (Fig. 18) are introduced to elucidate the pore size-dependent ink-bottle effect. The large capillary pores (group I in Fig. 18), mostly acting as ink-bottle pores, cannot be measured directly from standard MIP test. When the applied pressure exceeds a threshold level, corresponding to the threshold pore

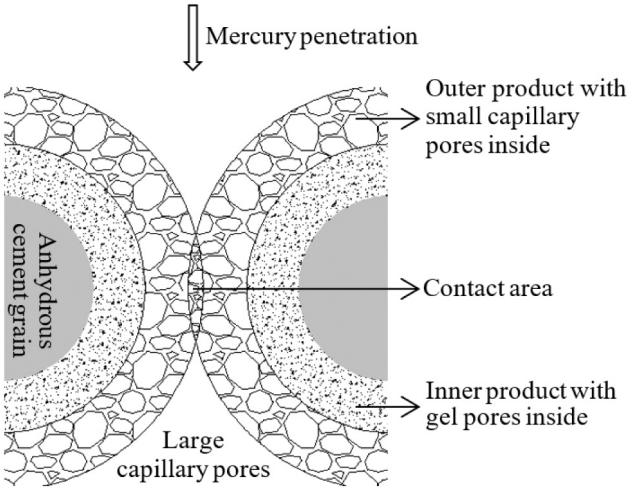

Fig. 17. Sketch of microstructure formed based on interactions between hydrating cement grains.

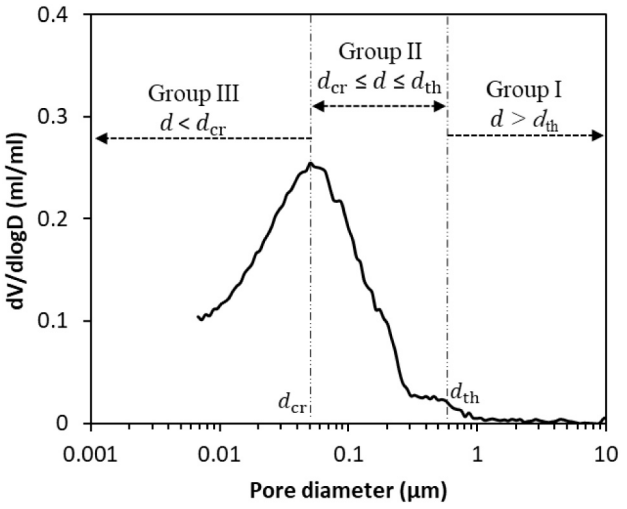

Fig. 18. Different pore groups based on the pore size distribution of cement paste obtained from standard MIP (d_{cr} - critical pore diameter; d_{th} - threshold pore diameter).

diameter d_{th}, the mercury starts to intrude the small capillary pores (group II in Fig. 18) and the interior large capillary pores, resulting in large ink-bottle effect and high α_{en} values. Once the critical pores (diameter d_{cr}) are intruded with mercury, a connected path is formed for the small capillary pores present in the contact area. Consequently, nearly all large capillary pores (group I) are assumed to be filled with mercury. With a further pressure increase, the throat pores ($d < d_{cr}$) are gradually filled with mercury and the subsequent ink-bottle pores are considered mostly as small capillary pores ($d \le d_{th}$), resulting in low α_{en} values.

The PDC-MIP approach [30] is based on the assumption that all the pores, regardless of pore sizes, are randomly connected. This reasoning needs to be reconsidered. The pore connections in cementitious systems may not be completely disordered, but follow basic principles that are related to the critical pore diameter d_{cr} and the threshold pore diameter d_{th}. The pores of group III ($d < d_{cr}$) primarily connect with small capillary pores ($d \le d_{th}$), and the ink-bottle volumes V_n^{ink} for $d < d_{cr}$ comprise mostly small capillary pores ($d \le d_{th}$). However, in the PDC-MIP data analysis, the volumes V_n^{ink} for $d < d_{cr}$ are allocated to the pore sizes from d_1 to d_{n-1} and, as a result, the amount of large capillary pores ($d > d_{th}$) tends to be overestimated and the amount of small capillary pores ($d \le d_{th}$) underestimated. The overestimation of large capillary pores ($d > d_{th}$) can become increasingly pronounced for the specimens with a later age or a lower w/b ratio, where stronger ink-bottle effect is present.

Improvements on the data analysis as described in the PDC-MIP approach [30] are necessary. It is more reasonable that allocations of the ink-bottle volume V_n^{ink} are performed with two stages according to the intrusion pore size d_n above or below the critical pore diameter d_{cr}, respectively. For $d_n \ge d_{cr}$, the ink-bottle volume V_n^{ink} is allocated to the pores with diameter larger than d_n, i.e. from d_1 to d_{n-1}. For $d_n < d_{cr}$, the ink-bottle volume V_n^{ink} is allocated to the pores with diameter from d_{th} to d_{n-1}.

6.3. Analysis of pore size distribution based on IEC-MIP

As discussed earlier, the PDC-MIP approach tends to overestimate the amount of large pores than actual situation. The mercury in throat pores is partially removed after the pressurization-depressurization cycle, and the concept of pore size dependent connectivity is not fully considered in the allocation of ink-bottle pore volume in the PDC-MIP approach. In response to these issues, IEC-MIP measurements and two-stage ink-bottle volume allocation method are implemented to gain a more truthful pore size distribution. The two-stage is set according to the applied pressure below or above the critical pressure, corresponding to the critical diameter d_{cr}.

In the *first* stage, the applied pressure is no larger than the critical pressure and mercury intrudes the pores with the size $d \ge d_{cr}$, and the ink-bottle volume V_i^{ink} at intrusion step i as illustrated in Fig. 5c is allocated to the pores from d_1 to d_{i-1}. In the *second* stage, after the critical pressure has been applied, mercury intrudes the pores with the size $d < d_{cr}$. The subsequent ink-bottle pores V_i^{ink} are all assumed as small capillary pores, and the ink-bottle volumes V_i^{ink} are allocated only to the small capillary pores from threshold diameter d_{th} to d_{i-1}. The threshold diameter d_{th} is determined as the onset for small capillary pores in the sense that there is an abrupt volume increase after the threshold pores are intruded with mercury according to the pore structure model given in Fig. 17.

It is defined that the threshold pores and critical pores start to be filled with mercury at step m and step k ($m < k$) respectively, i.e. $d_m = d_{th}$, $d_k = d_{cr}$. The first stage is from step 1 to step k and the second stage is from step $(k + 1)$ to the last step n. The two-stage pore size analysis is executed as follows.

Step 1: The $V_{1,1}$ is equal to V_1^{th} assuming that the largest pores do not have the ink-bottle effect.

$$V_{1,1} = V_1^{th} \tag{15}$$

Step 2: The ink-bottle volume V_2^{ink} is allocated to the pores larger than d_2, i.e. d_1.

$$V_{1,2} = V_{1,1} + V_2^{ink} \tag{16}$$

$$V_{2,2} = V_2^{th} \tag{17}$$

Step 3: The ink-bottle volume V_3^{ink} is allocated to the pores larger than d_3, i.e. d_1 and d_2.

$$V_{1,3} = V_{1,2} + V_3^{ink}\left(\frac{V_{1,2}}{V_{1,2} + V_{2,2}}\right) \tag{18}$$

$$V_{2,3} = V_{2,2} + V_3^{ink}\left(\frac{V_{2,2}}{V_{1,2} + V_{2,2}}\right) \tag{19}$$

$$V_{3,3} = V_3^{th} \tag{20}$$

Step k: The critical pores start to be filled with mercury and the ink-bottle volume V_k^{ink} is allocated to the pores from d_1 to d_{k-1}.

$$V_{i,k} = V_{i,k-1} + V_k^{ink}\left(\frac{V_{i,k-1}}{V_{1,k-1} + V_{2,k-1} + \cdots V_{k-1,k-1}}\right) \quad (i < k) \tag{21}$$

$$V_{k,k} = V_k^{\text{th}} \tag{22}$$

Step $k + j$: Since the critical pores have been filled with mercury, the ink-bottle volume V_{k+j}^{ink} is allocated to the pores with diameters from d_m to d_{k+j-1}.

$$V_{m,k+j} = V_{m,k+j-1} + V_{k+j}^{\text{ink}}\left(\frac{V_{m,k+j-1}}{V_{m,k+j-1} + V_{m+1,k+j-1} + \cdots + V_{k+j-1,k+j-1}}\right) (j \geq 1) \tag{23}$$

$$V_{i,k+j} = V_{i,k+j-1} + V_{k+j}^{\text{ink}}\left(\frac{V_{i,k+j-1}}{V_{m,k+j-1} + V_{m+1,k+j-1} + \cdots + V_{k+j-1,k+j-1}}\right) (m < i < k+j) \tag{24}$$

$$V_{k+j,k+j} = V_{k+j}^{\text{th}} \tag{25}$$

where $V_{i,\,k+j}$ is the volume of pores with the diameter of d_i calculated at step $k + j$.

Step n: The ink-bottle volume V_n^{ink} is allocated to pores with diameters from d_m to d_{n-1}.

$$V_{i,n} = V_{i,n-1} + V_n^{\text{ink}}\left(\frac{V_{i,n-1}}{V_{m,n-1} + V_{m+1,n-1} + \cdots + V_{n-1,n-1}}\right) (m \leq i < n) \tag{26}$$

$$V_{n,n} = V_n^{\text{th}} \tag{27}$$

The pore size distribution of 28-day OPC paste is recalculated using the two-stage pore size analysis as given in Eqs. (15)–(27), in combination with the data from IEC-MIP tests. Fig. 19 shows the result covering the pore diameter from 0.069 to 10 μm by following pressure Table 3. The size distribution of IEC-MIP is given primarily for the pores 0.069– 0.423 μm. A more detailed result for the pores 0.423– 10 μm can be plotted by implementing additional intrusion-extrusion steps between the pressure 0.15 and 3.4 MPa. In order for comparative analysis the pore size distribution results obtained from the 2nd pressurization of MIP, standard MIP, WMIP [9] and PDC-MIP [30], as well as from the well-known HYMOSTRUC3D [25], are presented. As indicated, the IEC-MIP shows clearly higher amount of small pores and lower amount of large pores as compared to PDC-MIP. The 2nd pressurization of MIP is known to measure the throat pores only and the volume of the throat pores below 0.1 μm is calculated as 11.3 %. If the ink-bottle effect is taken into account, the realistic volume of the small pores below 0.1 μm should be larger than 11.3 %. This value is 12.5 % as calculated following the measurement result from IEC-MIP, compared to a significantly lower value of 3.1 % as from PDC-MIP. The cumulative volume of small pores below 0.1 μm from IEC-MIP is reasonably acceptable by comparing with that from the 2nd pressurization of MIP. In addition, the cumulative volume of large pores above 0.5 μm appears to be consistent with that from WMIP. It is sensible to conclude that the IEC-MIP approach, together with the two-stage pore size analysis, is reliable for pore size identifications.

The 2nd pressurization of MIP seems applicable for determining the small pores of OPC paste after comparing with IEC-MIP. This makes sense by considering the low mercury entrapment of the small pores as can be seen in Fig. 9. This might not be the case however for the blended cement pastes that have high mercury entrapment for the small pores as addressed in Fig. 10. IEC-MIP measurements combining with microstructure-based mercury penetration model enable to provide trustworthy estimate of the pore size distribution in blended cement pastes.

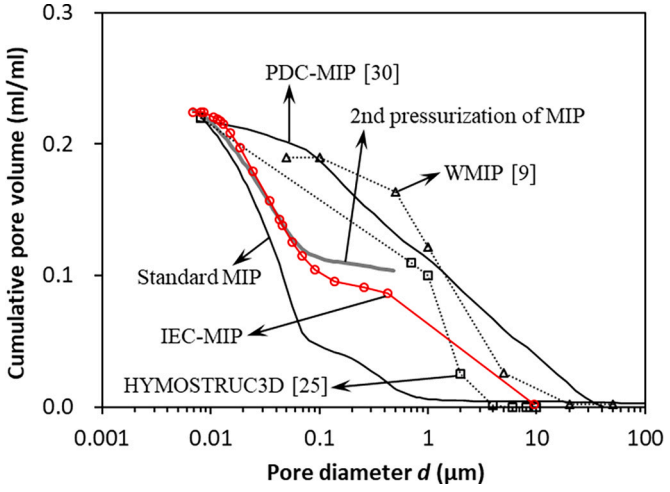

Fig. 19. Pore size distributions of the 28-day OPC paste based on different methods.

7. Concluding remarks

This work presents a further contribution on the topic of reliable characterizations of cementitious pore structure. It is found that the PDC-MIP approach of a previous report results in the ink-bottle pore volume to be overestimated, caused by the incomplete extrusion of mercury from throat pores. An improved measurement, i.e. intrusion-extrusion cyclic mercury porosimetry (IEC-MIP), is described and has proven to be trustworthy for capturing the distribution of ink-bottle pores in cementitious materials. Both the advancing and receding contact angles are not required for the IEC-MIP measurements to characterize the ink-bottle effect. According to the IEC-MIP tests of various cementitious pastes, the main findings are summarized as follows.

1) The ink-bottle effect exists in the whole pore size range of cementitious systems while it is pore size dependent and highly relies on the critical pore diameter. Different influences of blended materials on the ink-bottle effect are closely associated with their distinct roles in the large capillary pores during microstructure development.
2) The water-cement ratio and the age affect the total porosity of OPC pastes mainly by altering the effective porosity while the ink-bottle porosity differs slightly. The pastes with 30 % FA exhibit a small change with age for the ink-bottle porosity but a remarkable decrease for the effective porosity. Both effective porosity and ink-bottle porosity reduces clearly with age by including 70 % BFS. The minor addition of 5 % LP significantly enlarges the effective porosity but slightly alters the ink-bottle porosity.
3) The small pores of OPC pastes are highly interconnected. The reactive blends, either FA or BFS, can substantially reduce the connectivity of small pores. The large pores of cementitious materials are in general poorly connected.
4) The pore structure of BFS-blended cementitious systems is significantly coarsened with the addition of LP. Combining the alumina-rich FA with LP shows a synergistic effect in filling the capillary pores due to the formation of carboaluminate and bulky ettringite.
5) Two-stage pore size analysis method is proposed accounting for the role of critical pores in the distribution of ink-bottle pores. IEC-MIP measurements combining with microstructure-based mercury penetration model enable to provide trustworthy estimates of the pore size distribution of cementitious materials.
6) In future the construction materials should be selected on the basis of the contribution they can make to reach sustainability requirements. Different blends, no matter weak reactive or strong reactive nature, have distinct contributions to the refinement of pore structure.

CRediT authorship contribution statement

Yong Zhang: Conceptualization, Methodology, Formal analysis, Writing – original draft, Writing – review & editing. **Kai Wu**:

Investigation, Resources, Funding acquisition. **Zhengxian Yang**: Conceptualization, Data curation, Writing – review & editing. **Guang Ye**: Supervision, Validation, Writing – review & editing.

Declaration of competing interest

The authors declare that they have no known competing financial interests or personal relationships that could have appeared to influence the work reported in this paper.

Data availability

Data will be made available on request.

Acknowledgements

This research was financially supported by National Natural Science Foundation of China (51978171), Key Laboratory of Advanced Civil Engineering Materials (Tongji University), Ministry of Education (202102), Qishan Scholar (Overseas) Program of Fuzhou University (GXRC-19023), and Natural Science Foundation of Fujian Province, China (2020J01482). Valuable comments and suggestions from Prof. Jian Zhou (Hebei University of Technology, China) and Dr. Branko Šavija (Delft University of Technology, the Netherlands) are highly appreciated.

References

[1] J. Bao, J. Wei, P. Zhang, Z. Zhuang, T. Zhao, Experimental and theoretical investigation of chloride ingress into concrete exposed to real marine environment, Cem. Concr. Compos. 130 (2022), 104511.
[2] M. Wasim, T.D. Ngo, D. Law, A state-of-the-art review on the durability of geopolymer concrete for sustainable structures and infrastructure, Constr. Build. Mater. 291 (2021), 123381.
[3] M. Alexander, H. Beushausen, Durability, service life prediction, and modelling for reinforced concrete structures – review and critique, Cem. Concr. Res. 122 (2019) 17–29.
[4] R.D. Hooton, Future directions for design, specification, testing, and construction of durable concrete structures, Cem. Concr. Res. 124 (2019), 105827.
[5] Y. Zhang, Z. Yang, G. Ye, Dependence of unsaturated chloride diffusion on the pore structure in cementitious materials, Cem. Concr. Res. 127 (2020), 105919.
[6] M.C.G. Juenger, H.M. Jennings, The use of nitrogen adsorption to assess the microstructure of cement paste, Cem. Concr. Res. 31 (6) (2001) 883–892.
[7] D.N. Winslow, S. Diamond, A mercury porosimetry study of the evolution of porosity in Portland cement, J. Mater. 5 (1970) 564–585.
[8] K.L. Scrivener, Backscattered electron imaging of cementitious microstructures: understanding and quantification, Cem. Concr. Compos. 26 (2004) 935–945.
[9] K.L. Willis, A.B. Abell, D.A. Lange, Image-based characterization of cement pore structure using wood's metal intrusion, Cem. Concr. Res. 28 (12) (1998) 1695–1705.
[10] S. Hong, P. Liu, J. Zhang, F. Xing, B. Dong, Visual & quantitative identification of cracking in mortar subjected to loads using X-ray computed tomography method, Cem. Concr. Compos. 100 (2019) 15–24.
[11] A.C.A. Muller, K.L. Scrivener, A reassessment of mercury intrusion porosimetry by comparison with 1H NMR relaxometry, Cem. Concr. Res. 100 (2017) 350–360.
[12] J. Elsen, Microscopy of historic mortars—a review, Cem. Concr. Res. 36 (8) (2006) 1416–1424.
[13] L. Holzer, F. Indutnyi, P. Gasser, B. Münch, M. Wegmann, Three-dimensional analysis of porous BaTiO3 ceramics using FIB nanotomography, J. Microsc. 216 (1) (2010) 84–95.
[14] H.L. Ritter, L.C. Drake, Pore-size distribution in porous materials: pressure porosimeter and determination of complete macropore-size distributions, Ind. Eng. Chem. Anal. Ed. 17 (12) (1945) 782–786.
[15] L.C. Drake, H.L. Ritter, Macropore-size distributions in some typical porous substances, Ind. Eng. Chem. Anal. Ed. 17 (12) (1945) 787–791.
[16] P. Zwietering, H.L.T. Koks, Pore-size distribution of porous iron, Nat. 173 (1954) 683–684.
[17] H.G. Midgley, J.M. Illston, Some comments on the microstructure of hardened cement pastes, Cem. Concr. Res. 13 (1983) 197–206.
[18] R.A. Cook, Fundamentals of mercury intrusion porosimetry and its application to concrete materials science, MSc Thesis, Cornell University, 1991.
[19] S. Diamond, Mercury porosimetry: an inappropriate method for the measurement of pore size distributions in cement-based materials, Cem. Concr. Res. 30 (2000) 1517–1525.
[20] R. Kumara, B. Bhattacharjee, Assessment of permeation quality of concrete through mercury intrusion porosimetry, Cem. Concr. Res. 34 (2004) 321–328.
[21] B. Lubelli, D.A.M. de Winter, J.A. Post, R.P.J. van Hees, M.R. Drury, Cryo-FIB–SEM and MIP study of porosity and pore size distribution of bentonite and kaolin at different moisture contents, Appl. Clay Sci. 80–81 (2013) 358–365.
[22] Z. Gu, R. Goulet, P. Levitz, D. Ihiawakrim, O. Ersen, M.Z. Bazant, Mercury cyclic porosimetry: measuring pore-size distributions corrected for both pore-space accessivity and contact-angle hysteresis, J. Colloid Interface Sci. 599 (2021) 255–261.
[23] E.W. Washburn, The dynamics of capillary flow, Phys. Rev. 17 (1921) 273–283.
[24] F. Moro, H. Bőhni, Ink-bottle effect in mercury intrusion porosimetry of cement-based materials, J. Colloid Interface Sci. 246 (2002) 135–149.
[25] G. Ye, Experimental study and numerical simulation of the development of the microstructure and permeability of cementitious materials, Delft University of Technology, 2003. Ph.D. Thesis.
[26] H. Giesche, Mercury porosimetry: a general (practical) overview, Part. Part. Syst. Charact. 23 (2006) 9–19.
[27] A. Reverberi, G. Ferraiolo, A. Peloso, Experimental determination of the distribution function of the cylindrical macropores and the "ink bottle" pores in a porous system, Ann. Chim. 56 (12) (1966) 1552–1561.
[28] Q. Zeng, S. Chen, P. Yang, Y. Peng, J. Wang, C. Zhou, Z. Wang, D. Yan, Reassessment of mercury intrusion porosimetry for characterizing the pore structure of cement-based porous materials by monitoring the mercury entrapments with X-ray computed tomography, Cem. Concr. Compos. 113 (2020), 103726.
[29] J. Kaufmann, R. Loser, A. Leemann, Analysis of cement-bonded materials by multi-cycle mercury intrusion and nitrogen sorption, J. Colloid Interface Sci. 336 (2009) 730–737.
[30] J. Zhou, G. Ye, K. van Breugel, Characterization of pore structure in cement-based materials using pressurization–depressurization cycling mercury intrusion porosimetry (PDC-MIP), Cem. Concr. Res. 40 (2010) 1120–1128.
[31] C. Voigt, J. Hubálková, H. Giesche, C.G. Aneziris, Intrusion and extrusion mercury porosimetry measurements at Al2O3–C - influence of measuring parameter, Microporous Mesoporous Mater. 299 (2020), 110125.
[32] C.E. Salmas, G.P. Androutsopoulos, A novel pore structure tortuosity concept based on nitrogen sorption hysteresis data, Ind. Eng. Chem. Res. 40 (2001) 721–730.
[33] H.M. Jennings, S.K.J. Johnson, Simulation of microstructure development during the hydration of a cement compound, J. Am. Ceram. Soc. 69 (1986) 790–795.
[34] D.P. Bentz, E.J. Garboczi, Percolation of phases in a three-dimensional cement paste microstructural model, Cem. Concr. Res. 21 (1991) 325–344.
[35] P. Navi, C. Pignat, Simulation of cement hydration and the connectivity of the capillary pore space, Adv. Cement Based Mat. 4 (2) (1996) 58–67.
[36] P.K. Mehta, D. Manmohan, Pore size distribution and permeability of hardened cement pastes, in: Proceedings of the Seventh International Congress on the Chemistry of Cement, Paris 3, 1980, pp. 1–5 (7).
[37] P. Chindaprasirt, C. Jaturapitakkul, T. Sinsiri, Effect of fly ash fineness on compressive strength and pore size of blended cement paste, Cem. Concr. Compos. 27 (4) (2005) 425–428.
[38] P. Chindaprasirt, S. Rukzon, Pore structure changes of blended cement pastes containing fly ash, rice husk ash, and palm oil fuel ash caused by carbonation, J. Mater. Civ. Eng. 21 (11) (2009) 666–671.
[39] S. Diamond, Aspects of concrete porosity revisited, Cem. Concr. Res. 29 (8) (1999) 1181–1188.
[40] B. Lothenbach, G.L. Saout, E. Gallucci, K. Scrivener, Influence of limestone on the hydration of Portland cements, Cem. Concr. Res. 38 (2008) 848–860.
[41] H.J. Kuzel, H. Pollmann, Hydration of C3A in the presence of Ca(OH)2, CaSO4·2H20 and CaCO3, Cem. Concr. Res. 21 (1991) 885–895.
[42] B. Lothenbach, P. Durdzinski, K. de Weerdt, Thermogravimetric analysis, in: K. L. Scrivener, R. Snellings, B. Lothenbach (Eds.), A Practical Guide to Microstructural Analysis of Cementitious Materials, CRC Press Taylor & Francis Group, Boca Raton, 2015, pp. 177–211.
[43] K. Scrivener, R. Snellings, B. Lothenbach, A Practical Guide to Microstructural Analysis of Cementitious Materials, CRC Press Taylor & Francis Group, Florida, USA, 2016.
[44] K. de Weerdt, M.B. Haha, G.L. Saout, K.O. Kjellsen, H. Justnes, B. Lothenbach, Hydration mechanisms of ternary Portland cements containing limestone powder and fly ash, Cem. Concr. Res. 41 (2011) 279–291.
[45] K. van Breugel, Numerical simulation of hydration and microstructural development in hardening cement-based materials, Ph.D. thesis, Delft University of Technology, 1991.
[46] H.M. Jennings, Refinements to colloid model of C-S-H in cement: CM-II, Cem. Concr. Res. 38 (2008) 275–289.